Thermocapillary convection in a cylinder with a strong non-uniform axisymmetric magnetic field

By YU YU KHINE AND JOHN S. WALKER

Department of Mechanical and Industrial Engineering, University of Illinois,
Urbana, IL 61801, USA

This paper treats a surface-tension-driven liquid-metal flow in a cylinder with a steady externally applied non-uniform axisymmetric magnetic field. The top boundary consists of an annular free surface around a solid disk, modelling the Czochralski growth of silicon crystals. A radial temperature gradient produces a decrease of the surface tension from the disk edge to the vertical cylinder wall. The magnetic flux density is sufficiently large that inertial effects and convective heat transfer are negligible. First we present large-Hartmann-number asymptotic solutions for magnetic fields with either a non-zero or a zero axial component at the free surface. The asymptotic solutions indicate that a purely radial magnetic field at the free surface represents a singular limit of more general magnetic fields. Secondly we present numerical solutions for arbitrary values of the Hartmann number, and we treat the evolution of the thermocapillary convection as the axial magnetic field at the free surface is changed continuously from the full field strength to zero.

1. Background

In the Czochralski (CZ) process, a single crystal is grown from a liquid melt contained in a crucible which is surrounded by a heater, as sketched in figure 1. Here we consider the CZ growth of dislocation-free silicon crystals with silica (SiO_2) crucibles. Approximately 80% of the integrated circuits for computers and other electronic devices are produced on wafers sliced from CZ silicon crystals (Zulehner 1983). Erosion of the crucible introduces oxygen into the melt. The oxygen either evaporates from the melt's free surface as SiO or enters the crystal. A small amount of oxygen strengthens the crystal and prevents warpage of wafers during the thermal cycles needed to produce an integrated circuit (Hoshi *et al.* 1985). Under typical conditions, 98% of the oxygen entering the melt must evaporate from the free surface in order to achieve the desired oxygen concentration in the crystal (Series & Hurle 1991).

The diffusion coefficient for oxygen in molten silicon is extremely small, namely $D = 5 \times 10^{-8} \text{ m}^2 \text{ s}^{-1}$, according to Hirata & Hoshikawa (1992). Only melt passing very close to the crucible surface acquires oxygen, and only melt passing very close to the free surface loses oxygen by evaporation. The upward velocity v_z near the vertical crucible wall is proportional to the strength of the buoyant convection, which is driven by the 30 to 60 K temperature difference between the crystal–melt interface at 1683 K and the hottest point on the vertical crucible wall (Sabhapathy & Salcudean 1991). The radially outward velocity v_r near the crucible bottom depends primarily on the centrifugal pumping associated with the crucible rotation. In general, an increase in the crucible's angular velocity produces an increase in v_r near the crucible bottom and an
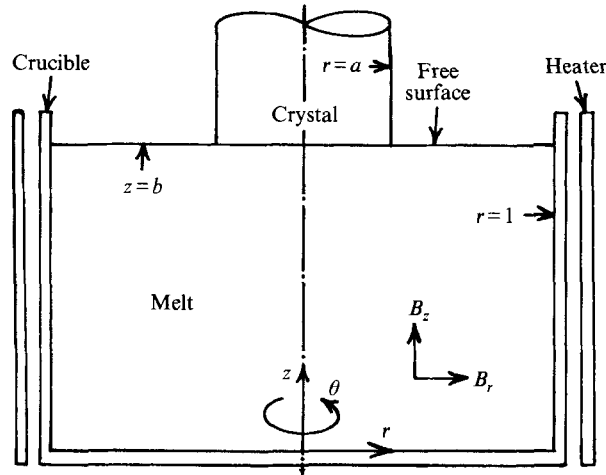
FIGURE 1. Model of Czochralski crystal growth with a non-uniform axisymmetric magnetic field. Dimensions and coordinates are normalized by the inside radius of the crucible, R_c. The radial and axial components of the magnetic field, B_r and B_z, are normalized by the root-mean-squared magnetic flux density, with the mean taken over the volume of the melt.

associated increase in the transport of oxygen from the crucible bottom to the bulk of the melt (Hirata & Hoshikawa 1989b). Some crucible rotation is needed to smooth out the effects of small deviations from axisymmetry in the heater.

The radially inward velocity at the free surface is proportional to the strength of the thermocapillary convection, which is driven by the decrease of the surface tension from the cold crystal edge to the hot crucible. With a strong thermocapillary convection, the melt which has passed close to the crucible surface loses its oxygen by evaporation before it reaches the bulk of the melt or the crystal–melt interface, so that the crystal has the desired low oxygen concentration. The radially outward velocity near the crystal face is driven by the centrifugal pumping associated with the rotation of the crystal and ensures radially uniform distributions of oxygen and dopants such as phosphorus or boron in the crystal (Series & Hurle 1991).

The electrical conductivities of molten silicon and mercury are nearly equal, so that the melt motion can be controlled by an externally applied magnetic field. The many numerical and experimental studies of CZ silicon growth with magnetic fields were recently reviewed by Series & Hurle (1991) and by Langlois, Kim & Walker (1993). The first benefit of a magnetic field is the elimination of turbulence and all large-scale periodicity in the melt motion (Hirata & Hoshikawa 1992). Temporal fluctuations in the heat transfer and oxygen or dopant transport from the melt to the growing crystal produce many microscopic structural defects and microscopic concentration variations in the crystal (Kuroda, Kozuka & Takano 1984). Recent advances in integrated-circuit manufacturing have dramatically increased the number of transistors per cm^2 of wafer surface and have led to the need to eliminate microscopic defects and concentration variations in the CZ crystals from which the wafers are sliced.

A melt velocity v in the presence of a magnetic field B produces an induced electric field, $v \times B$. The induced electric field drives an electric current density j, which produces an electromagnetic (EM) body force, $j \times B$, opposing the component of v which is perpendicular to B. Therefore, the EM forces opposing melt velocities which are perpendicular or parallel to the magnetic field are large or zero, respectively. All melt circulations involve both flows along and across the magnetic field. However, if

the predominant direction of the flow in a circulation is perpendicular or parallel to the local magnetic field, then the EM suppression of the circulation is large or small, respectively.

Initial experiments and modelling efforts focused on uniform magnetic fields which were either vertical (axial) or horizontal (transverse). An axial magnetic field does not disturb the axisymmetry of the heat and mass transfer to the crystal, but it strongly suppresses the desirable thermocapillary convection and centrifugal pumping near the crystal face because these radial motions are predominantly perpendicular to the axial magnetic field. Crystals grown in axial magnetic fields frequently have (i) excessive oxygen concentrations due to the EM suppression of the thermocapillary convection needed to ensure that 98 % of the oxygen evaporates, and (ii) extremely non-uniform radial distributions of oxygen due to the EM suppression of the crystal-face centrifugal pumping (Ravishankar, Braggins & Thomas 1990). There are other reasons for high oxygen concentrations with axial magnetic fields, e.g. the temperature of the crucible must be increased with an axial field, so that the rate of crucible ablation is increased. Hjellming & Walker (1986, 1987) showed that (i) the magnitude of the thermocapillary convection varies as B_0^{-2}, (ii) the magnitude of the crystal-face centrifugal-pumping circulation varies as B_0^{-3}, and (iii) the buoyant velocity near the vertical crucible wall varies as $B_0^{-3/2}$, where B_0 is the magnetic flux density of the uniform axial magnetic field. Sabhapathy & Salcudean (1991) presented numerical calculations which confirmed that the asymptotic solutions of Hjellming & Walker are valid for a typical CZ process with $B_0 > 0.2$ T.

A transverse magnetic field has a component which is perpendicular to the vertical crucible wall, except along two vertical lines. Therefore, it strongly suppresses the buoyant convection along the vertical wall and reduces oxygen transport from the crucible to the bulk of the melt. Walker & Williams (1994, 1995) showed that (i) the radial thermocapillary velocity near the free surface varies as $B_0^{-1/2}$, and (ii) the radial centrifugal-pumping velocity near the crystal face varies as B_0^{-1}, for a uniform transverse magnetic field. With such weak EM suppression of thermocapillary convection and centrifugal pumping, crystals grown with a uniform transverse magnetic field have low and radially uniform oxygen concentrations (Ravishankar *et al.* 1990). Oxygen concentrations increase as the crucible rotation rate is increased, since centrifugal pumping near the crucible bottom provides the primary oxygen transport from the crucible surface to the bulk of the melt. Unfortunately the melt motion with a transverse magnetic field is far from axisymmetric (Walker & Williams 1993, 1994), and the associated convective heat transfer produces a strongly non-axisymmetric heat flux to the crystal. A point on the rotating crystal face experiences a large fluctuation in heat flux which produces highly undesirable periodic variations in the crystal structure, called thermal striations (Ravishankar *et al.* 1990). Therefore both axial and transverse uniform magnetic fields produce unacceptable crystals.

In order to gain the benefits of a magnetic field without the disadvantages of either a transverse or axial uniform field, several researchers have proposed a particular non-uniform axisymmetric magnetic field called a cusp field (Hirata & Hoshikawas 1989 *a*; Series, 1989; Hicks, Organ & Riley 1989). A cusp field is produced by two identical solenoids which generate vertical magnetic fields in opposite directions and which are placed around the CZ furnace symmetrically above and below the plane of the crystal–melt interface and free surface. The four objectives of the cusp field are to produce: (i) a purely radial magnetic field near the free surface so that there is minimal EM suppression of the thermocapillary convection needed for oxygen evaporation, (ii) a very small radial magnetic field near the crystal–melt interface so that there is

minimal EM suppression of the crystal-face centrifugal pumping needed for radial uniformity of oxygen and dopants in the crystal, (iii) a radial magnetic field at the vertical crucible wall so that there is strong EM suppression of the vertically upward buoyant convection along this wall, and (iv) an axial magnetic field at the crucible bottom so that there is strong EM suppression of the centrifugal pumping associated with the crucible rotation. While we refer to oxygen and dopants together, their radial uniformity in the crystal depends on different mechanisms. Most dopants are rejected at the crystallization interface, so that elevated concentrations develop inside a thin diffusion boundary layer, and the radial uniformity within this very thin layer is important. Oxygen is not rejected at crystallization, so that it does not have a diffusion layer, and its radial uniformity depends on mixing in the melt, i.e. on motion on a much larger physical scale. All experimental results to date for cusp fields are very positive (Series 1989; Hirata & Hoshikawa 1989a, b). The only disadvantage of a cusp field produced by two solenoids outside the CZ furnace is that the maximum magnetic flux density in the melt is very small compared to that elsewhere, so that most of the magnetic field is wasted. This problem could be greatly diminished by putting solenoids inside the furnace, close to the heaters and crystal, but there is currently disagreement about the possibility of putting solenoids inside the furnace (Series & Hurle 1991).

Most modelling of melt motion in non-uniform axisymmetric magnetic fields to date has focused on the cusp field (Hicks *et al.* 1989; Sabhapathy & Salcudean 1991; Hirata & Hoshikawa 1992). Hjellming, Tolley & Walker (1993) treated centrifugal pumping with a strong non-uniform axisymmetric magnetic field with a non-zero axial magnetic field at the plane of the free surface and crystal face, so that their analysis applies for all cases except the cusp field. In crystals grown without a magnetic field or with a cusp field and with the free surface at the zero-axial-field plane throughout crystal growth, the oxygen transport to the crystal decreases during crystal growth, producing an undesirable longitudinal variation of the oxygen concentration in the crystal. Hirata & Hoshikawa (1989b) showed experimentally that a uniform longitudinal distribution of oxygen could be achieved by moving the free surface away from the zero-axial-field plane when half of the crystal is grown. During the second half of the process, the non-zero axial field at the free surface suppresses thermocapillary convection and the associated oxygen evaporation, thus leaving more oxygen to enter the crystal. There were no adverse effects on the radial oxygen and dopant distributions in the crystal.

This paper treats only the thermocapillary convection. Analyses are developed for all possible non-uniform axisymmetric magnetic fields, and results are presented for one family of such fields. The results show the evolution of the flow as the magnetic field is changed continuously from a uniform axial field to a cusp field.

2. Problem formulation

With any magnetic field, the magnitudes of the radial and axial velocities decrease as the characteristic magnetic flux density B_0 is increased, so that the characteristic velocity U varies as some inverse power of B_0. The characteristic ratio of the EM body-force term to the inertial term in the Navier–Stokes equation is the interaction parameter, $N = \sigma B_0^2 R_c / \rho U$, where σ and ρ are the electrical conductivity and density of the melt, while R_c is the inside radius of the crucible which serves as the characteristic length. We assume that N is sufficiently large that all inertial terms are negligible, except the radial centrifugal force associated with the azimuthal velocity. We also assume that the Péclét number, $Pe = \rho c U R_c / k$, is sufficiently small that convective heat transfer is negligible, where c and k are the specific heat and thermal conductivity

of the melt. With these two assumptions, the melt motions due to thermocapillarity, buoyancy and centrifugal pumping can be treated independently and then superposed in order to treat mass transport of oxygen and dopants. The mass Péclét number, $Pe_m = UR_c/D$, is always very large because the diffusion coefficients D are so small.

The assumption that convective heat transfer is negligible is probably only valid for the strongest magnetic fields being considered for commercial silicon crystal growth. For weak or moderate magnetic field strengths, the melt motions due to thermocapillarity, buoyancy and centrifugal pumping are coupled, and numerical treatment of complete problems is needed (Hicks *et al.* 1989; Hirata & Hoshikawa 1992; Sabhapathy & Salcudean 1991). The present asymptotic treatment with decoupled flows and the numerical treatment of complete problems complement each other: the former provides physical insights which can guide process optimization, while the latter provides more accurate predictions for specific cases and defines the limitations of the asymptotic results.

Here we only treat the thermocapillary convection with various steady non-uniform axisymmetric magnetic fields which have only radial and axial components, B_r and B_z. Since the magnetic Reynolds number, $R_m = \mu_p \sigma UR_c$, is always very small, the components of B satisfy

$$\frac{\partial B_r}{\partial r} + \frac{B_r}{r} + \frac{\partial B_z}{\partial z} = 0, \quad \frac{\partial B_r}{\partial z} = \frac{\partial B_z}{\partial r}, \tag{1a, b}$$

where μ_p is the magnetic permeability. We choose the root-mean-squared value of the magnetic flux density for B_0, where the mean is taken over the volume of the melt. Therefore the dimensionless field is scaled by the condition

$$\int_0^1 \int_0^b (B_r^2 + B_z^2)\, r\, dz\, dr = 0.5b, \tag{2}$$

where b is the instantaneous dimensionless melt depth, as indicated in figure 1. For the flow problem, B_r and B_z are known functions of r and z.

The thermocapillary convection only involves radial and axial velocities, so that the dimensionless governing equations are

$$\frac{\partial p}{\partial r} = B_z j_\theta + Ha^{-2} \left(\frac{\partial^2 v_r}{\partial r^2} + \frac{1}{r} \frac{\partial v_r}{\partial r} + \frac{\partial^2 v_r}{\partial z^2} - \frac{v_r}{r^2} \right), \tag{3a}$$

$$\frac{\partial p}{\partial z} = -B_r j_\theta + Ha^{-2} \left(\frac{\partial^2 v_z}{\partial r^2} + \frac{1}{r} \frac{\partial v_z}{\partial r} + \frac{\partial^2 v_z}{\partial z^2} \right), \tag{3b}$$

$$j_\theta = B_r v_z - B_z v_r, \quad \frac{1}{r} \frac{\partial}{\partial r}(rv_r) + \frac{\partial v_z}{\partial z} = 0, \tag{3c, d}$$

where p and j_θ are the pressure and azimuthal electric current density, normalized by $\sigma UB_0^2 R_c$ and σUB_0, respectively, while $Ha = B_0 R_c (\sigma/\mu)^{1/2}$ is the Hartmann number and μ is the melt's viscosity. Here $(3a, b)$ are the radial and axial components of the inertialess Navier–Stokes equation with the EM body force and $(3c)$ is the azimuthal component of Ohm's law with the induced electric field and zero azimuthal static electric field because of axisymmetry. Since the electric current in the melt is azimuthal, the electrical conductivities of the crucible, crystal and atmosphere have no effect on the thermocapillary convection.
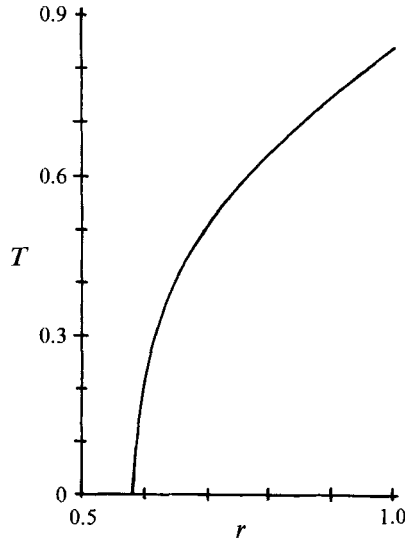
FIGURE 2. Dimensionless temperature at the free surface, $T(r, b)$, for $a = 0.59$ and $b = 1$.

We use the bulk flow approximation which assumes that the crystal–melt interface and the free surface are planar and lie in the same horizontal plane. In reality, the free surface has a meniscus rising to the particular angle associated with constant-diameter crystal growth, while the crystal–melt interface may be slightly convex or concave.

The boundary conditions at the crucible surfaces and crystal–melt interface are $v_r = v_z = 0$, at $z = 0$ for $0 < r < 1$, at $r = 1$ for $0 < z < b$, and at $z = b$ for $0 < r < a$, where a is the dimensionless radius of the crystal. We assume that the surface tension γ is a linearly decreasing function of the dimensional temperature T^*, so that $d\gamma/dT^*$ is a negative constant. For the thermocapillary convection we choose

$$U = (-d\gamma/dT^*)(\Delta T^*)_0/B_0 R_c(\sigma\mu)^{1/2},$$

where $(\Delta T^*)_0$ is the characteristic temperature difference in the melt. With this characteristic velocity, the boundary conditions at the free surface are

$$\frac{\partial v_r}{\partial z} = -Ha\frac{\partial T}{\partial r}, \quad v_z = 0 \quad \text{at} \quad z = b \quad \text{for} \quad a < r < 1, \qquad (4a, b)$$

where the dimensionless temperature $T = (T^* - 1683 \text{ K})/(\Delta T^*)_0$. Here 1683 K is the melting temperature of silicon, so that $T = 0$ at the crystal–melt interface. For the thermal problem, we neglect convective heat transfer, we assume that there is no heat transfer through the crucible bottom, we assume that there is a uniform heat flux q from the vertical crucible wall to the melt, and we include radiation from the free surface (Hjellming & Walker 1987). We use 0.3 for the radiative emissivity of the free surface (Sabhapathy & Salcudean 1991). With $(\Delta T^*)_0 = qR_c/k$, $\partial T/\partial r = 1$ at $r = 1$. The dimensionless temperature at the free surface for $a = 0.59$ and $b = 1$ is presented in figure 2.

The neglect of inertial effects and of convective heat transfer is only valid for relatively large values of B_0, for which Ha is also large, e.g. Ha is approximately 600 for a typical CZ process with $B_0 = 0.2$ T. In §3, we present asymptotic solutions for $Ha \gg 1$ and for magnetic fields with non-zero values of B_z at the free surface. In §4, we

present the corresponding asymptotic solution for the cusp field with $B_z = 0$ at $z = b$. The two asymptotic solutions are very different with $O(Ha^{-1})$ and $O(1)$ dimensionless circulations for the cases in §3 and §4, respectively. Therefore the large-Hartmann-number asymptotic solutions indicate that the cusp field represents a singular limit, and that perfect alignment between the free surface and the local magnetic field is needed in order to gain the benefits of a cusp field. In §5, we present numerical solutions for arbitrary values of Ha, and we show that the cusp field does not represent a singular limit for realistic values of Ha. For $Ha = 100$ or 400, the circulations with modest misalignments are only slightly less than those for perfect alignment. The asymptotic solutions provide physical insights into the numerical results. For the cusp field, the asymptotic solution is essentially realized for $Ha \geqslant 200$. On the other hand, for a magnetic field with a small angle between the local field direction and the plane of the free surface, the asymptotic solution in §3 would not be realized until Ha became much larger than the values encountered in actual magnetic CZ crystal growth. Of course, the §3 solution is realized for modest values of Ha when the angle between the local field and the free surface is not small, e.g. an axial field.

3. Large-Hartmann-number solutions for a non-zero axial magnetic field at the free surface

The asymptotic analyses presented in this section parallel those presented by Hjellming *et al.* (1993) for centrifugal pumping with various non-uniform, axisymmetric magnetic fields.

3.1. *Hartmann-layer solution for the first magnetic field*

First we consider magnetic fields with $B_z > 0$, $B_r > 0$ and $\partial B_z / \partial z < 0$ throughout the melt, i.e. the magnetic field lines fringe radially outward and the axial field strength decreases as z increases from 0 to b. The flow subregions for $Ha \gg 1$ are shown in figure 3. There are two interior layers, I1 and I2, which lie along the magnetic field lines through the ends of the free surface, i.e. through the crystal edge at $r = a$, $z = b$, and through the free-surface–crucible contact at $r = 1$, $z = b$. These interior layers have an $O(Ha^{-1/2})$ dimensionless thickness and separate the three inviscid cores, C1, C2 and C3. Since there is a non-zero normal component of B at each boundary, there is a Hartmann layer H with an $O(Ha^{-1})$ thickness between each boundary and the adjacent core or interior layer.

In cores C1 and C3, and in the adjacent Hartmann layers, v_r, v_z, and j_θ are zero, while p is constant, to all orders in Ha^{-1}. Therefore the thermocapillary convection is confined to the core C2, the two interior layers, the free-surface Hartmann layer and the middle Hartmann layer on the crucible bottom. In the core C2, all variables are $O(Ha^{-1})$, but in the free-surface Hartmann layers, v_r and j_θ are $O(1)$, while v_z and p are $O(Ha^{-1})$. For the free-surface Hartmann layer, the solution of (3*a*, *c*) which satisfies (4*a*) and matches the core is

$$v_{rh} = -[B_z(r,b)]^{-1} \frac{\partial T}{\partial r}(r,b) \exp[B_z(r,b)Z], \qquad (5a)$$

$$j_{\theta h} = \frac{\partial T}{\partial r}(r,b) \exp[B_z(r,b)Z], \qquad (5b)$$

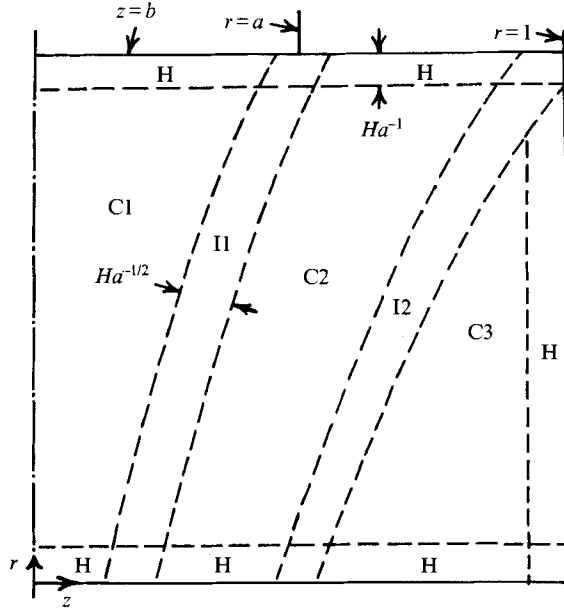where $Z = Ha(z-b)$ is the stretched axial coordinate and $O(Ha^{-1})$ terms are neglected.

FIGURE 3. Flow subregions for $Ha \gg 1$ and for a magnetic field with $B_z > 0$, $B_r > 0$, and $\partial B_z / \partial z < 0$ throughout the melt.

The dimensionless total radial flow inside the free-surface Hartmann layer at each radius is

$$Q_h(r) = -2\pi Ha^{-1}[B_z(r,b)]^{-2} r \frac{\partial T}{\partial r}(r,b), \tag{6}$$

neglecting $O(Ha^{-2})$ terms. From figure 2, the quantity $r \partial T / \partial r$ at $z = b$ increases from 1.0 to 1.63 as r decreases from 1.0 to 0.65. If B_z is uniform over the free surface, the radially inward flow inside the free-surface Hartmann layer increases as r decreases from 1 to a, which implies an $O(Ha^{-1})$ axial velocity from the core C2 to this Hartmann layer.

3.2. *Core solution for the first magnetic field*

For the core C2 and both interior layers, we use an orthogonal curvilinear coordinate system (Ψ, θ, Φ), where Ψ and Φ are the stream and potential functions for the dimensionless axisymmetric magnetic field B satisfying (1), so that

$$B_r = \frac{\partial \Phi}{\partial r} = -\frac{1}{r} \frac{\partial \Psi}{\partial z}, \quad B_z = \frac{\partial \Phi}{\partial z} = \frac{1}{r} \frac{\partial \Psi}{\partial r}.$$

Hjellming *et al.* (1993) presented the metrics and other details of this system. With Ψ and Φ as the independent variables, $r(\Psi, \Phi)$ and $z(\Psi, \Phi)$ are the radial and axial coordinates and $B(\Psi, \Phi) = (B_r^2 + B_z^2)^{1/2}$ is the local dimensionless magnetic field strength. In a $\theta = $ constant vertical plane, the unit vectors

$$\hat{n} = B^{-1}(B_z \hat{r} - B_r \hat{z}), \quad \hat{t} = B^{-1}(B_r \hat{r} + B_z \hat{z})$$

are perpendicular and parallel to the magnetic field at each point, where $\hat{r}, \hat{\theta}, \hat{z}$ are the unit vectors for the cylindrical coordinates. Therefore $\hat{n}, \hat{\theta}, \hat{t}$ are the right-handed, orthogonal unit vectors for the (Ψ, θ, Φ) coordinates, and the magnetic field at each point is $B = B(\Psi, \Phi) \hat{t}$.

In the core C2, $v = Ha^{-1}(v_{nc}\hat{n} + v_{tc}\hat{t})$, $j_\theta = Ha^{-1}j_{\theta c}$ and $p = Ha^{-1}p_c$, neglecting $O(Ha^{-2})$ terms. From (3a, b), p_c is independent of Φ, i.e. the pressure $p_c(\Psi)$ is constant along each magnetic field line. Then (3) gives

$$j_{\theta c} = r\frac{dp_c}{d\Psi}, \quad v_{nc} = -\frac{r}{B}\frac{dp_c}{d\Psi}, \qquad (7a, b)$$

$$\frac{\partial}{\partial\Phi}\left(\frac{v_{tc}}{B}\right) = \frac{\partial}{\partial\Psi}\left(\frac{r^2}{B^2}\frac{dp_c}{d\Psi}\right). \qquad (7c)$$

The total volumetric flow across any axisymmetric $\Psi = $ constant surface is zero. In the middle Hartmann layer on the crucible bottom, v_r and v_z are $O(Ha^{-1})$ and $O(Ha^{-2})$, respectively, so that its contribution to the flow is $O(Ha^{-2})$. Therefore the $O(Ha^{-1})$ outward core velocity v_{nc} across the surface must cancel the radially inward flow (6) inside the free-surface Hartmann layer. On each $\Psi = $ constant magnetic field line, $\Phi_b(\Psi)$ and $\Phi_f(\Psi)$ are the values of Φ where this magnetic field intersects the bottom and free surface, respectively, i.e. $z(\Psi, \Phi_b(\Psi)) = 0$ and $z(\Psi, \Phi_f(\Psi)) = b$. In addition, $A(\Psi)$ is the value of the quantity $B_z^{-2}r\,\partial T/\partial r$ at the point where this magnetic field intersects the free surface, i.e.

$$A(\Psi) = \left\{[B_z(r, b)]^{-2}r\frac{\partial T}{\partial r}(r, b)\right\}_{r=r(\Psi, \Phi_f(\Psi))}.$$

Conservation of mass gives the pressure gradient at each magnetic field line,

$$\frac{dp_c}{d\Psi} = -A(\Psi)\left\{\int_{\Phi_b(\Psi)}^{\Phi_f(\Psi)} r^2 B^{-2}\,d\Phi\right\}^{-1}. \qquad (8)$$

Along each magnetic field line, all the variables are proportional to the radial temperature gradient where this field line intersects the free surface. For the present magnetic field, r increases and B decreases as we move along a field line from the bottom to the free surface. Therefore (7b) indicates that v_{nc} is small near the bottom and large near the free surface. Along each field line, (7c) can be integrated from $\Phi = \Phi_b(\Psi)$ to any Φ, where matching the bottom Hartmann layer gives

$$v_{tc} = -r^2 B^{-1}\frac{d\Phi_b}{d\Psi}\frac{dp_c}{d\Psi} \quad \text{at} \quad \Phi = \Phi_b(\Psi).$$

The $O(Ha^{-1}) \times O(Ha^{-1/2})$ intersection region at $r = a$, $z = b$ accepts a radially inward flow from the free-surface Hartmann layer and delivers it to the interior layer I1 at $z = b$. This flow descends inside I1 and enters the core C2 with the distribution dictated by (7b), (8) evaluated at $\Psi = \Psi(a, b)$. The flow entering C2 from the upper part of I1 flows directly to the free-surface Hartmann layer. The flow entering C2 from the lower part of I1 spreads out as it crosses C2 until enters I2 with the distribution dictated by (7b), (8) evaluated at $\Psi = \Psi(1, b)$. This flow ascends inside I2 to enter the $O(Ha^{-1}) \times O(Ha^{-1/2})$ intersection region at $r = 1$, $z = b$, where it turns to enter the free-surface Hartmann layer at $r = 1$. The structure of the two interior layers is somewhat complicated by the variations of B and r with Φ along these layers, but the structure is qualitatively similar to that treated in detail by Hjellming & Walker (1987) for the interior layer at $r = a$ for a uniform axial magnetic field. The only additional characteristics of the interior layers which we will cite in §5 are that the flow enters I1 or leaves I2 as a point source or sink at $z = b$ and that the streamlines spread out roughly as parabolas as z decreases from b.
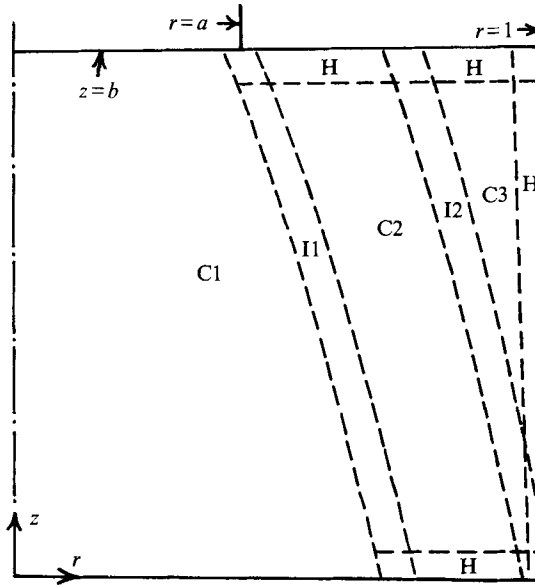
FIGURE 4. Flow subregions for $Ha \gg 1$ and for a magnetic field with $B_z > 0$, $B_r < 0$, and $\partial B_z / \partial z > 0$ throughout the melt.

3.3. *Second magnetic field*

Next we consider a magnetic field with $B_z > 0$, $B_r < 0$, and $\partial B_z / \partial z > 0$ throughout the melt, i.e. the magnetic field lines fringe inward and the axial magnetic field strength increases as z increases from 0 to b. The flow subregions for $Ha \gg 1$ are shown in figure 4. The interior layer I2 now lies along the magnetic field line through the crucible corner at $r = 1$, $z = 0$. The core C1 and adjacent Hartmann layers are again stagnant to all orders, while the solutions in the free-surface Hartmann layer, core C2 and interior layer I1 are the same. Now the core C3 is not stagnant, and the $O(Ha^{-1})$ variables here are given by (7), (8) with $\Phi_b(\Psi)$ replaced by $\Phi_v(\Psi)$ which is the value of Φ where each $\Psi =$ constant magnetic field line intersects the vertical crucible wall, i.e. $r(\Psi, \Phi_v(\Psi)) = 1$. The interior layer I2 is quite different – there is no $O(Ha^{-1})$ flow inside it, the $O(Ha^{-1})v_{nc}$ is continuous across it, and the only role of this much weaker layer is to match a discontinuity between the values of v_{tc} in cores C2 and C3. Even this weak discontinuity is an artifact of our simplified model because actual crucibles have rounded junctions between the actually curved bottoms and the vertical walls. There is an $O(Ha^{-1}) \times O(Ha^{-1})$ region at the free-surface–crucible contact at $r = 1$, $z = b$, which accepts an $O(Ha^{-1})$ flow from C3 and delivers it to the free-surface Hartmann layer, so that C3 sees this region as a sink.

3.4. *Third magnetic field*

The third magnetic field considered in this section is that produced by a solenoid around the heater and an opposing solenoid very close to the crystal. The upper solenoid produces a downward magnetic field under the crystal and adjacent part of the free surface, as sketched in figure 5. This field turns outward and upward in the melt. The field from the lower solenoid fringes outward to intersect the outer part of the free surface and the vertical crucible wall. The dividing magnetic field line, $\Psi = 0$, intersects the $r = 0$ axis where $B = 0$. The subregions of the flow for $Ha \gg 1$ and three typical magnetic field lines are shown in figure 5.
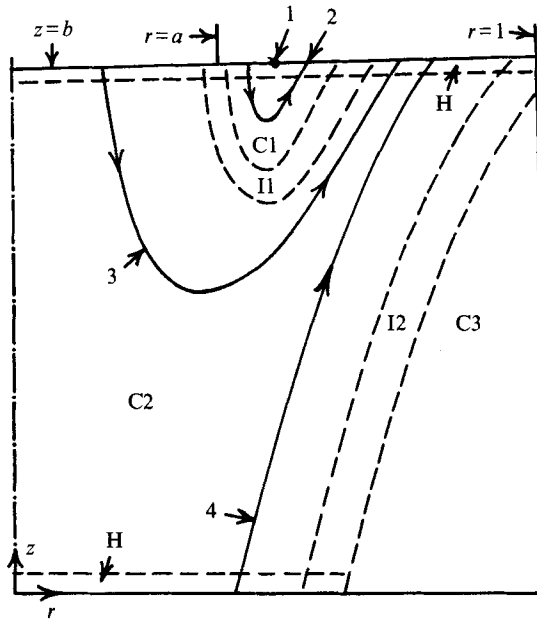
FIGURE 5. Flow subregions for $Ha \gg 1$ and for the magnetic field produced by a solenoid around the heater and another opposing solenoid near the crystal. Here 1 indicates the point where the magnetic field is tangent to the free surface, while 2, 3 and 4 indicate the three different types of magnetic field lines in the melt.

Here we refer to the solution for our first magnetic field whose subregions were presented in figure 3. For our third field, the core C3 and adjacent Hartmann layers are again stagnant to all orders. Except at the point 1 in figure 5 where $B_z = 0$, the solution for the free-surface Hartmann layer is given by (5), (6) with B_z replaced by $|B_z|$ and with sgn(B_z) added to (5b). At the point 1, there is a region with $\Delta r = O(Ha^{-1/3})$ and $\Delta z = O(Ha^{-2/3})$ which matches the singularity in the Hartmann-layer solution (5), (6) as $B_z \rightarrow 0$ (Roberts 1967). The structures of the interior layer I2 and intersection region at $r = 1$, $z = b$ are the same. In the core C2, there are two types of magnetic field lines, denoted as 3 and 4 in figure 5. Field line 4 intersects the crucible bottom and free surface, so that (7), (8) apply. Field line 3 intersects the crystal face and free surface, so that (7), (8) apply with $\Phi_b(\Psi)$ replaced by $\Phi_s(\Psi)$, which is the value of Φ where each magnetic field line intersects the crystal face i.e. $z(\Psi, \Phi_s(\Psi)) = b$. We might expect a discontinuity across the $\Psi = 0$ magnetic field line because $\Psi = 0^-$ intersects the crystal face while $\Psi = 0^+$ intersects the crucible bottom. However, the radii in (7), (8) indicate that all variables vanish along the axis where the abrupt field change occurs, so that there are no discontinuities in the interior of C2.

The field line 2 in core C1 intersects the free surface twice. The velocity v_{nc} across this field line is proportional to the difference between the radially inward flows Q_h inside the free-surface Hartmann layer at the two ends of this field line, while the velocity v_{tc} along this field line depends on the variation of Q_h between adjacent field lines. From (6), Q_h might well have nearly equal values at the ends of each magnetic field line in C1, but the magnitude of Q_h decreases in both directions from a maximum near the point 1 to a minima adjacent to I1. Therefore the flow in C1 and the adjacent part of the free-surface Hartmann layer consists primarily of strong local inward flow inside the Hartmann layer with return flow along the magnetic field lines in C1. In reality, Ha is not sufficiently large for $Ha^{-1/3}$ to be very small, so that the region with $\Delta r =$

$O(Ha^{-1/3})$ and $\Delta z = O(Ha^{-2/3})$ probably extends over most of the core C1, and viscous effects reduce the strong local circulation from that predicted by (6)–(8). Nevertheless, we expect strong circulation in the pocket above the field line through the crystal edge. The radially inward flow in the free-surface Hartmann layer adjacent to C2 continues across the free surface inside the Hartmann layer to $r = a$ and then travels around I1 from the crystal edge to enter C2 with distribution dictated by (7), (8) with $\Phi_b(\Psi)$ replaced by $\Phi_s(\Psi)$ and evaluated at $\Psi = \Psi(a, b)$.

4. Large-Hartmann-number solution for a purely radial magnetic field at the free surface

Here we treat the cusp field for which B_r and B_z are even and odd functions of $(z - b)$, respectively. The thermocapillary convection is now confined to a top layer which has an $O(Ha^{-1/2})$ thickness and which lies adjacent to the free surface and crystal face at $z = b$. Everywhere else in the melt, $v_r = v_z = j_\theta = p = 0$ to all orders in Ha^{-1}. As the magnetic field for figure 3 approaches the cusp field, the free-surface Hartmann layer, the core C2 and both interior layers merge into the top layer at $z = b$ and the stagnant core C3 spreads over the rest of the melt.

The top layer for the cusp field and the interior layers in §3 have the same $O(Ha^{-1/2})$ thickness and the same force balance: (i) an $O(1)$ velocity across the magnetic field produces an electromagnetic body force which is balanced by the gradient of the $O(Ha^{-1/2})$ pressure normal to the field, and (ii) the resultant pressure gradient parallel to the magnetic field is balanced by the viscous stresses and accelerates the flow to an $O(Ha^{1/2})$ velocity parallel to the field. The primary difference between the top layer here and the interior layers in §3 is that the top layer is a semi-infinite layer which is driven by the thermocapillary stress on its top boundary, while the interior layers are doubly infinite layers which emanate from singularities. For example, layer I1 in figure 3 is driven by a mass source at $r = a$, $z = b$; as the flow descends from this source inside the layer, it spreads and is fed into the core C2.

We introduce the stretched axial coordinate $\zeta = Ha^{1/2}(z - b)$ and the stream function $\psi_t(r, \zeta)$ for the $O(1)$ circulation in the top layer. In this layer

$$B_r = B_r(r, b) + O(Ha^{-1}), \quad B_z = Ha^{-1/2}\zeta\frac{\partial B_z}{\partial z}(r, b) + O(Ha^{-3/2}),$$

$$v_r = \frac{1}{r}Ha^{1/2}\frac{\partial\psi_t}{\partial\zeta} + O(Ha^{-1/2}), \quad v_z = -\frac{1}{r}\frac{\partial\psi_t}{\partial r} + O(Ha^{-1}),$$

$$j_\theta = -\frac{1}{r}B_r(r, b)\frac{\partial\psi_t}{\partial r} - \frac{\zeta}{r}\frac{\partial B_z}{\partial z}(r, b)\frac{\partial\psi_t}{\partial\zeta} + O(Ha^{-1}).$$

We derive the equation governing ψ_t by introducing these expressions into $(3a, b)$ and by cross-differentiating to eliminate the $O(Ha^{-1/2})$ pressure. The result is

$$[B_r(r, b)]^2\frac{\partial^2\psi_t}{\partial r^2} + 2\zeta B_r(r, b)\frac{\partial B_z}{\partial z}(r, b)\frac{\partial^2\psi_t}{\partial r\,\partial\zeta} + \zeta^2\left[\frac{\partial B_z}{\partial z}(r, b)\right]^2\frac{\partial^2\psi_t}{\partial\zeta^2}$$

$$+ \zeta\left\{B_r(r, b)\frac{\partial^2 B_z}{\partial r\,\partial z}(r, b) + \frac{\partial B_z}{\partial z}(r, b)\left[\frac{\partial B_z}{\partial z}(r, b) - \frac{2}{r}B_r(r, b)\right]\right\}\frac{\partial\psi_t}{\partial\zeta}$$

$$- B_r(r, b)\left[\frac{\partial B_z}{\partial z}(r, b) + \frac{3}{r}B_r(r, b)\right]\frac{\partial\psi_t}{\partial r} = \frac{\partial^4\psi_t}{\partial\zeta^4}, \tag{9}$$

for $0 < r < 1$ and $-\infty < \zeta < 0$. The boundary conditions at the crystal–melt interface and at the free surface are

$$\psi_t = 0, \quad \frac{\partial \psi_t}{\partial \zeta} = 0 \quad \text{at} \quad \zeta = 0 \quad \text{for} \quad 0 < r < a, \tag{10a, b}$$

$$\psi_t = 0, \quad \frac{\partial^2 \psi_t}{\partial \zeta^2} = -r \frac{\partial T}{\partial r}(r, b) \quad \text{at} \quad \zeta = 0 \quad \text{for} \quad a < r < 1. \tag{10c, d}$$

There is a Hartmann-layer-like region with $\Delta r = O(Ha^{-1})$ and $\Delta z = O(Ha^{-1/2})$ between the top layer and the vertical crucible wall. This region matches any value of the $O(1)$ top-layer v_z as long as the $O(Ha^{1/2})$ top-layer $v_r = 0$ at $r = 1$. Therefore

$$\psi_t = 0 \quad \text{at} \quad r = 1. \tag{11}$$

Matching the stagnant core gives

$$\psi_t \to 0 \quad \text{as} \quad \zeta \to -\infty. \tag{12}$$

In §5, we will consider magnetic fields with

$$B_r = Cr, \quad B_t = 2C(\alpha b - z), \tag{13a, b}$$

which is the local field produced by a pair of identical opposing solenoids whose radius and distance from the symmetry plane at $z = \alpha b$ are both much larger than the melt dimension R_c. Several authors (Hirata & Hoshikawa 1989a; Hicks *et al.* 1989; Sabhapathy & Salcudean 1991) have computed magnetic fields for specific solenoid pairs outside the CZ furnace and the field variations are quite close to (13) because the outside radius of the furnace is much larger than R_c. With our normalization, (2) gives

$$C = [\tfrac{1}{2} + 4b^2(\alpha^2 - \alpha + \tfrac{1}{3})]^{-1/2}. \tag{14}$$

The cusp field corresponds to $\alpha = 1$, while the fields for figures 3 and 4 correspond to $\alpha > 1$ and $\alpha < 0$, respectively. Since we will compare the asymptotic solution in this section with the arbitrary-Hartmann-number solutions in §5, we use (13), (14) with $\alpha = b = 1$, so that

$$B_r(r, b) = Cr, \quad \frac{\partial B_z}{\partial z}(r, b) = -2C, \quad C = (\tfrac{6}{11})^{1/2}. \tag{15}$$

For our numerical solution, we truncate the domain at $\zeta = -d$, and we replace the matching condition (12) with the symmetry conditions

$$\psi_t = 0, \quad \frac{\partial^2 \psi_t}{\partial \zeta^2} = 0 \quad \text{at} \quad \zeta = -d. \tag{16}$$

We found that $d = 6$ is sufficiently large that all derivatives of ψ_t are essentially zero at $\zeta = -d$. We solved (9)–(11), (15), (16) with a Chebyshev spectral collocation method. Since there is a discontinuity at $r = a$ between the boundary conditions (10b, d) at $\zeta = 0$, we used a weighted Galerkin method to satisfy these conditions, which gives much better results than a collocation method. The series solution had 25 terms each in the radial and axial directions.

The streamlines are presented in figure 6. The radially inward flow close to the free
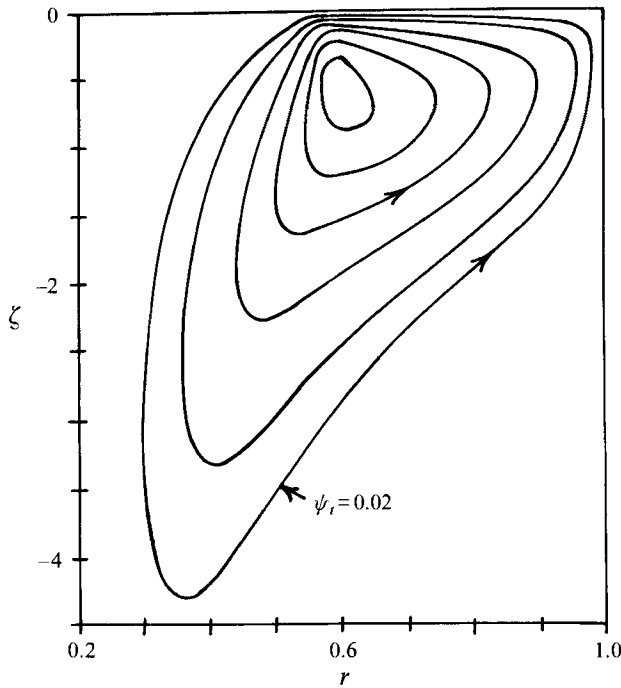
FIGURE 6. Streamlines for a cusp magnetic field and for $Ha \gg 1$.
Here $\psi_t = 0.02$ and $0.04k$ for $k = 1$ to 5.

surface turns downward at the crystal edge. The circulation is completed by an upward and radially outward flow which tries to follow the magnetic field lines. In the top layer, the stream function for the magnetic field is $\Psi = -Ha^{-1/2}Cr^2\zeta$. Therefore the streamline $\psi_t = 0.02$ closely follows the magnetic field line from $r = 0.5$, $\zeta = -4$ toward its intersection with the crucible at $r = 1$, $\zeta = -1$.

The maximum value of ψ_t for this field is 0.222, so that the large-Hartmann-number solution for this cusp field predicts that the dimensionless circulation approaches an $O(1)$ value of 0.222 as $Ha \to \infty$. This result contrasts with the §3 result that the dimensionless circulation approaches zero as Ha^{-1} when $Ha \to \infty$, as long as there is any non-zero axial magnetic field at the free surface.

5. Arbitrary-Hartmann-number solutions

We introduce the stream function $\psi(r, z)$ where

$$v_r = \frac{1}{r}\frac{\partial \psi}{\partial z}, \quad v_z = -\frac{1}{r}\frac{\partial \psi}{\partial r}.$$

Then (1), (3) give

$$B_r^2 \frac{\partial^2 \psi}{\partial r^2} + 2B_r B_z \frac{\partial^2 \psi}{\partial r \partial z} + B_z^2 \frac{\partial^2 \psi}{\partial z^2} + \left(B_z \frac{\partial B_r}{\partial z} - B_r \frac{\partial B_z}{\partial z} - \frac{3}{r} B_r^2\right)\frac{\partial \psi}{\partial r}$$

$$+ \left(B_z \frac{\partial B_z}{\partial z} + B_r \frac{\partial B_r}{\partial z} - \frac{2}{r} B_r B_z\right)\frac{\partial \psi}{\partial z}$$

$$= Ha^{-2}\left(\frac{\partial^4 \psi}{\partial r^4} - \frac{2}{r}\frac{\partial^3 \psi}{\partial r^3} + \frac{3}{r^2}\frac{\partial^2 \psi}{\partial r^2} - \frac{3}{r^3}\frac{\partial \psi}{\partial r} + 2\frac{\partial^4 \psi}{\partial r^2 \partial z^2} - \frac{2}{r}\frac{\partial^3 \psi}{\partial r \partial z^2} + \frac{\partial^4 \psi}{\partial z^4}\right). \quad (17)$$
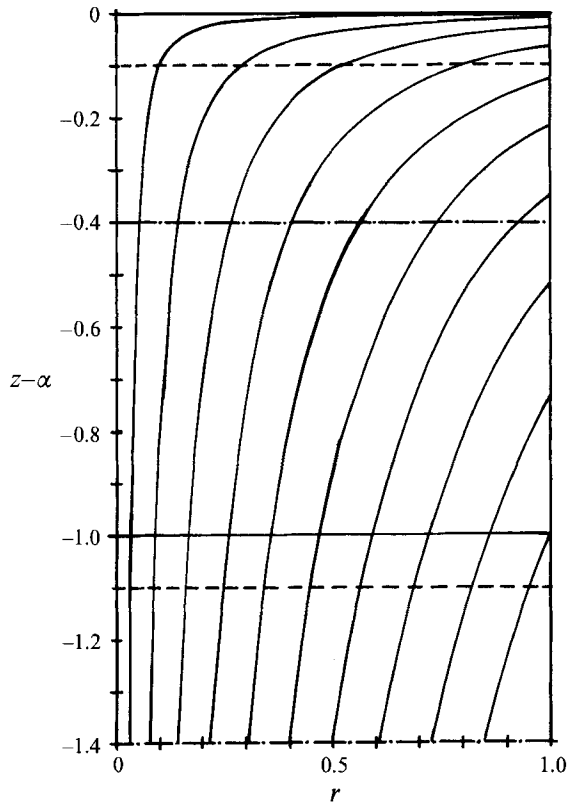
FIGURE 7. Magnetic field lines for $b = 1$, with the magnetic plane of symmetry at $z = \alpha$ and with the melt between $z = 0$ and $z = 1$. Field lines in the melt: (i) for $\alpha = 1.0$ between the solid lines at $z - \alpha = 0$ and -1, (ii) for $\alpha = 1.1$ between the dashed lines at $z - \alpha = -0.1$ and -1.1, (iii) for $\alpha = 1.4$ between the dot-dashed lines at $z - \alpha = -0.4$ and -1.4, and (iv) for a $= -0.4$ between the dot-dashed lines, inverted in z.

Here $B_r(r, z)$ and $B_z(r, z)$ are known variable coefficients. The boundary conditions are

$$\psi = 0, \quad \frac{\partial \psi}{\partial z} = 0 \quad \text{at} \quad z = 0 \quad \text{and at} \quad z = b \quad \text{for} \quad 0 < r < a, \quad (18a, b)$$

$$\psi = 0, \quad \frac{\partial \psi}{\partial r} = 0 \quad \text{at} \quad r = 1, \quad (18c, d)$$

$$\psi = 0, \quad \frac{\partial^2 \psi}{\partial z^2} = -rHa\frac{\partial T}{\partial r} \quad \text{at} \quad z = b \quad \text{for} \quad a < r < 1. \quad (18e, f)$$

We have solved (17), (18) numerically with essentially the same Chebyshev spectral collocation method used for the top layer in §4. Again we used a weighted Galerkin method for the discontinuous boundary conditions $(18b, f)$ at $z = b$. For larger values of Ha, many more terms in the spectral series are needed in order to resolve the Hartmann layers. For $Ha = 400$, the series had 25 terms in the radial direction and 50 terms in the axial direction.

We present results for the magnetic field (13), (14) with various values of α, with $b = 1$, with $a = 0.59$, and with the $T(r, b)$ in figure 2. We consider five magnetic fields: (i) a uniform axial magnetic field with $B_r = 0$ and $B_z = 1$, corresponding to $\alpha \to \infty$, (ii)
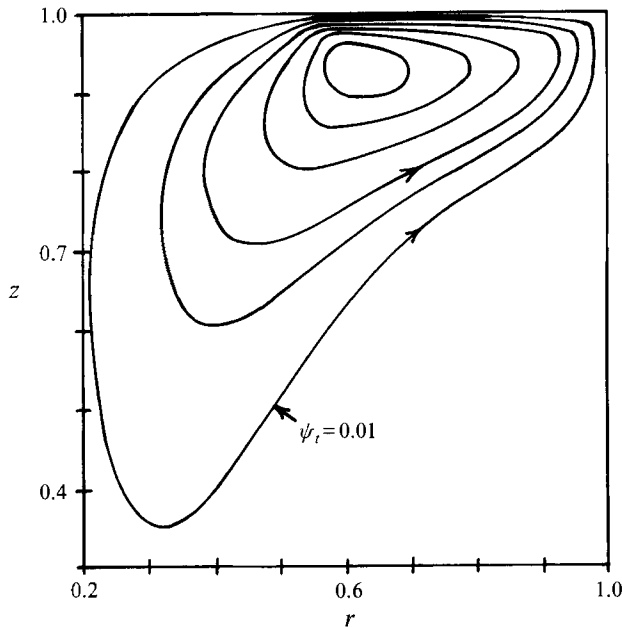
FIGURE 8. Streamlines for the cusp magnetic field and for $Ha = 100$. Here $\psi_t = 0.01$, 0.03 and $0.05 + 0.04k$ for $k = 0$ to 3.

a cusp field for $\alpha = 1$, (iii) a slight misalignment between B and the free surface for $\alpha = 1.1$, (iv) a modest misalignment for $\alpha = 1.4$, and (v) a figure-4 field with the largest B_z at the free surface for $\alpha = -0.4$. The magnetic field lines in the melt for the non-uniform-field cases are presented in figure 7. For $\alpha \geqslant b$, the dimensionless magnetic-field strength increases from B_{min} at $r = 0$, $z = b$ to B_{max} at $r = 1$, $z = 0$. For three of the cases in figure 7, B_{min} is 0, 0.133 and 0.396, while B_{max} is 1.65, 1.60 and 1.47 for $\alpha = 1.0$, 1.1 and 1.4, respectively.

For the cusp field with $\alpha = 1.0$, the maximum values of ψ are 0.0625, 0.157, 0.194, 0.220 and 0.222 for $Ha = 10$, 50, 100, 200 and 400, respectively. Since the asymptotic value for $Ha \gg 1$ is 0.222, we conclude that the asymptotic solution is realized for $Ha \geqslant 200$. The streamlines for $Ha = 100$ are presented in figure 8. After a vertical rescaling with $Ha^{1/2} = 10$, the streamlines in figures 6 and 8 are very similar. The streamlines for $Ha = 200$ and 400 are virtually identical to those in figure 8 with the appropriate compression toward $z = 1$.

For $\alpha = 1.1$ with a slight misalignment between B and the free surface, the streamlines for $Ha = 100$ and 400 are very similar to those for $\alpha = 1$. The maximum values of ψ are 0.177 and 0.197 for $Ha = 100$ and 400, respectively. The asymptotic solution in §3 predicts that the circulation with any non-zero value of $B_z(r, b)$ should vary as Ha^{-1}, but as Ha is increased from 100 to 400, the circulation for $\alpha = 1.1$ increases by 11% rather than decreasing by 75%. In a plot of circulations versus Ha, that for $\alpha = 1.0$ asymptotes to 0.222 for $Ha > 200$, while that for $\alpha = 1.1$ reaches a maximum at some value of Ha greater than 400, and then decreases, ultimately approaching zero as Ha^{-1}. For $Ha < 400$, the only evidence of this difference between the circulations for $\alpha = 1.0$ and 1.1 is that the circulations for $\alpha = 1.1$ are 9.0% and 11.3% less than those for $\alpha = 1.0$ for $Ha = 100$ and 400, respectively. While both circulations are increasing, the difference between them is also increasing. For a typical CZ process with $B_0 < 0.5$T, $Ha < 1500$. We conclude that the asymptotic solution in
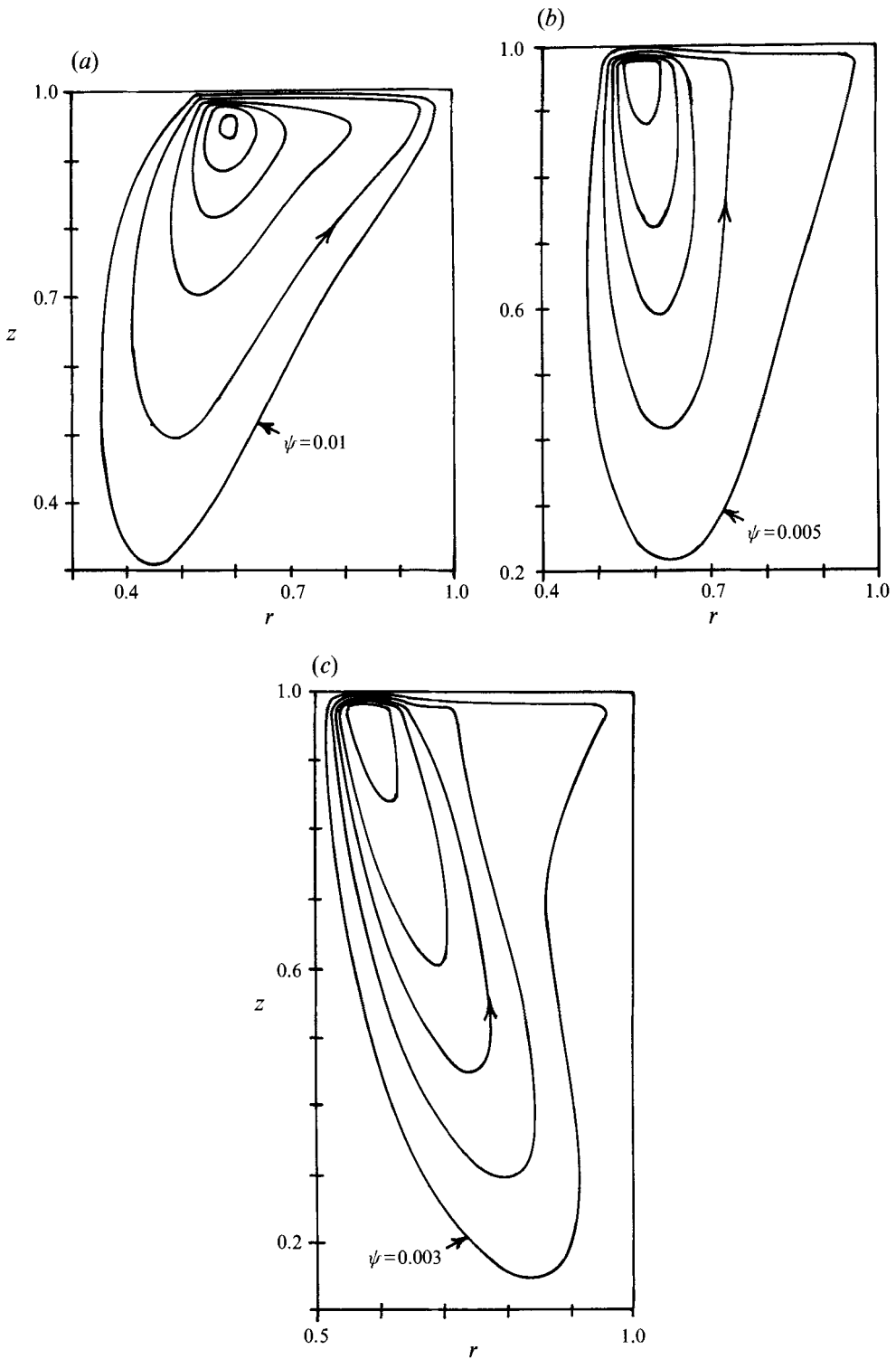
FIGURE 9. Streamlines for $Ha = 100$. (a) $\alpha = 1.4$; $\psi = 0.01$ and $0.02k$ for $k = 1$ to 5. (b) Uniform axial magnetic field ($\alpha \to \infty$): $\psi = 0.005k$ for $k = 1$ to 4 and $\psi = 0.03$. (c) $\alpha = -0.4$: $\psi = 0.003k$ for $k = 1$ to 4 and $\psi = 0.018$.

§3 is not realized in practice for slight misalignments between B and the free surface, and that the circulation is not radically less than that for perfect alignment.

The streamlines for $\alpha = 1.4$, for a uniform axial magnetic field ($\alpha \to \infty$), and for $\alpha = -0.4$ are presented in figure 9 for $Ha = 100$. The magnetic fields for $\alpha = 1.4$ and $\alpha = -0.4$ correspond to those for figures 3 and 4, respectively. The streamlines follow the magnetic field lines as the field changes from fringing outward in figure 3 to a uniform field and then to fringing inward in figure 4. The interior layers I1 and I2 in figure 3 are evident in figure 9(a). For I1, all the flow enters at $r = a$, $z = b$, spreads as it flows downward inside I1, and then enters the core C2. The four inner streamlines in figure 9(a) cross the core C2 and enter the Hartmann layer at the free surface. The two outer streamlines converge inside the layer I2 toward the corner at $r = 1$, $z = b$. The magnetic field lines in figure 7 show that $\alpha = -0.4$ is a special case for figure 4 because the magnetic field line through the crystal corner at $r = a$, $z = b$ also passes through the crucible corner at $r = 1$, $z = 0$. Therefore the interior layers I1 and I2 in figure 4 are merged into a single interior layer with a core bounded by this interior layer, the free surface and the vertical crucible wall. Figure 9(c) shows the flow inside the merged interior layers from the crystal edge at $r = a$, $z = b$ toward the crucible corner at $r = 1$, $z = 0$. The melt flows vertically upward across the core from the interior layer to the Hartmann layer at the free surface. For $\alpha = -0.4$, the streamlines penetrate further toward the bottom as (7b) would predict with a weaker field near the bottom. The maximum values of ψ are 0.1065, 0.0426 and 0.0275 for the circulations in figures 9(a), 9(b) and 9(c), respectively. Equation (6) predicts that these values should vary as $[B_z(r, b)]^{-2}$, but the actual results for $Ha = 100$ vary more like $[B_z(r, b)]^{-1}$. Since $B_z(r, b) = 0.396$ and 1.387 for $\alpha = 1.4$ and -0.4, rescaling of the uniform-field circulation with $[B_z(r, b)]^{-1}$ gives 0.1075 and 0.0307 for $\alpha = 1.4$ and -0.4, respectively. For $Ha = 400$, the circulations of these three cases scale approximately as $[B_z(r, b)]^{-3/2}$. We are approaching the asymptotic solution in §3, but we have not reached it for $Ha = 400$.

As Ha is increased from 100 to 400, the maximum values of ψ decrease from 0.1065 to 0.078 for $\alpha = 1.4$ and from 0.0426 to 0.0202 for a uniform axial field. While the circulation does not increase as it does for $\alpha = 1.1$, it does not decrease as rapidly as Ha^{-1} either. For a uniform $B_z(r, b)$, (6) indicates that the circulation is proportional to the value of $\partial T / \partial r$ at the point where the free-surface Hartmann layer H intersects the interior layer I1 in figure 3, i.e. at $r = a + O(Ha^{-1/2})$. Figure 2 indicates that $\partial T / \partial r$ increases rapidly as r approaches a. As Ha is increased, the circulation decreases because it is confined to the Hartmann layer with $O(Ha^{-1})$ thickness, but it is also driven by a larger maximum value of $\partial T / \partial r$ at a point closer to $r = a$. The circulation will not decrease as Ha^{-1} until $Ha^{-1/2}$ is so small that the interior layer I1 has negligible thickness, as assumed in the asymptotic solution in §3.

6. Conclusions

One of the disadvantages of a uniform axial magnetic field is its strong suppression of the thermocapillary convection which carries the melt to the free surface so that the oxygen can evaporate. A cusp magnetic field with only a radial component at the free surface should produce less suppression of the desirable convection. The asymptotic solutions in §§3 and 4 for non-zero and zero axial magnetic fields at the free surface indicate that the thermocapillary convections should vary as B_0^{-2} and B_0^{-1}, respectively, where B_0 is the root-mean-squared magnetic flux density in the melt. A uniform axial magnetic field is a special case of the non-uniform fields treated in §3. The ratio of the

circulation for a cusp field to that for a uniform axial magnetic field is 4.56 or 11.02 for $Ha = 100$ or 400, where Ha is the Hartmann number based on B_0. The results in §5 show that the large-Hartmann-number asymptotic solution for the cusp field is realized for $Ha \geqslant 200$, but that for the uniform axial field still deviates from the actual flow for $Ha = 400$. The asymptotic solutions in §§3 and 4 indicate that perfect alignment between the local magnetic field and the plane of the free surface is required in order to achieve the benefits of a cusp field. However, the results in §5 indicate that the circulation for a slight misalignment with the dimensionless $B_z = 0.133$ at the free surface is only moderately less than that for perfect alignment for the entire range of magnetic flux densities used for Czochralski crystal growth.

The analyses in §§3 and 4 assume that $B_z(r, b)$ is $O(1)$ and zero, respectively. The essential characteristics of the top layer in §4 are the same for any $B_z(r, b)$ which is $O(Ha^{-1/2})$. For $Ha^{-1/2} \ll B_z(r, b) \ll 1$, the top layer has a thickness which is $O([HaB_z(r, b)]^{-1})$ and is essentially a Hartmann layer, so that the analysis of §3 applies. One could bridge the gap between the two asymptotic solutions in §§3 and 4 by setting $B_z(r, b) = \beta Ha^{-1/2}$, where β is an $O(1)$ parameter. The solutions in §§3 and 4 would represent the limits of this more general asymptotic solution as $\beta \to \infty$ and as $\beta \to 0$, respectively. From the results for $Ha = 400$ in §5, we see that as β is increased from 0 ($\alpha = 1.0$) to 2.7 ($\alpha = 1.1$) or to 7.9 ($\alpha = 1.4$), the magnitude of the melt circulation is reduced by 11% or by 65%, respectively. We conclude that misalignments between the local magnetic field and free surface produce only small flow reductions as long as the dimensionless magnetic field component which is perpendicular to the free surface is less than roughly $3Ha^{-1/2}$.

REFERENCES

HICKS, T. W., ORGAN, A. E. & RILEY, N. 1989 Oxygen transport in magnetic Czochralski growth of silicon with a non-uniform magnetic field. *J. Cryst. Growth* **94**, 213–228.

HIRATA, H. & HOSHIKAWA, K. 1989*a* Silicon crystal growth in a cusp magnetic field. *J. Cryst. Growth* **96**, 747–755.

HIRATA, H. & HOSHIKAWA, K. 1989*b* Homogeneous increase in oxygen concentration in Czochralski silicon crystals by a cusp magnetic field. *J. Cryst. Growth* **98**, 777–781.

HIRATA, H. & HOSHIKAWA, K. 1992 Three-dimensional numerical analyses of the effects of a cusp magnetic field on the flows, oxygen transport and heat transfer in a Czochralski silicon melt. *J. Cryst. Growth* **125**, 181–207.

HJELLMING, L. N., TOLLEY, P. A. & WALKER, J. S. 1993 Melt motion in a Czochralski crystal puller with a non-uniform, axisymmetric magnetic field: isothermal motion. *J. Fluid Mech.* **249**, 1–34.

HJELLMING, L. N. & WALKER, J. S. 1986 Melt motion in a Czochralski crystal puller with an axial magnetic field: isothermal motion. *J. Fluid Mech.* **164**, 237–273.

HJELLMING, L. N. & WALKER, J. S. 1987 Melt motion in a Czochralski crystal puller with an axial magnetic field: motion due to buoyancy and thermocapillarity. *J. Fluid Mech.* **182**, 335–368.

HOSHI, K., ISAWA, N., SUZUKI, T. & OHKUBO, Y. 1985 Czochralski silicon crystals grown in a transverse magnetic field. *J. Electrochem. Soc. Solid-State Sci. Tech.* **132**, 693–700.

KURODA, E., KOZUKA, H. & TAKANO, Y. 1984 The effects of temperature oscillations at the growth interface on crystal perfection. *J. Cryst. Growth* **68**, 613–623.

LANGLOIS, W. E., KIM, K. M. & WALKER, J. S. 1993 Hydromagnetic flows and effects on Czochralski crystals. *J. Cryst. Growth* **126**, 352–372.

RAVISHANKAR, P. S., BRAGGINS, T. T. & THOMAS, R. N. 1990 Impurities in commercial-scale magnetic Czochralski silicon: axial versus transverse magnetic fields. *J. Cryst. Growth* **104**, 617–628.

ROBERTS, P. H. 1967 Singularities of Hartmann layers. *Proc. R. Soc. Lond.* A **300**, 94–107.

SABHAPATHY, P. & SALCUDEAN, M. E. 1991 Numerical study of Czochralski growth of silicon in an axisymmetric magnetic field. *J. Cryst. Growth* **113**, 164–180.

SERIES, R. W. 1989 Effect of a shaped magnetic field on Czochralski silicon growth. *J. Cryst. Growth* **97**, 92–98.

SERIES, R. W. & HURLE, D. T. J. 1991 The use of magnetic fields in semiconductor crystal growth. *J. Cryst. Growth* **113**, 305–328.

WALKER, J. S. & WILLIAMS, M. G. 1994 Centrifugal pumping during Czochralski silicon growth with a strong transverse magnetic field. *J. Cryst. Growth* **137**, 32–36.

WALKER, J. S. & WILLIAMS, M. G. 1995 Thermocapillary convection during Czochralski growth of a silicon crystal with a uniform, transverse magnetic field. *J. Materials Process. Manuf. Sci.* (submitted).

ZULEHNER, W. 1983 Czochralski growth of silicon. *J. Cryst. Growth* **65**, 189–213.